Recursive Deep Prior Video: A super resolution algorithm for time-lapse microscopy of organ-on-chip experiments

RECURSIVE DEEP PRIOR VIDEO: A SUPER RESOLUTION ALGORITHM FOR TIME-LAPSE MICROSCOPY OF ORGAN-ON-CHIP EXPERIMENTS *

Pasquale Cascarano
Department of Mathematics
University of Bologna
Piazza di Porta S. Donato 5, Bologna, 40126, Italy

Maria Colomba Comes
Department of Electronic Engineering
University of Tor Vergata
Via del Politecnico 1,00133, Rome, Italy
maria.colomba.comes@uniroma2.it

Arianna Mencattini
Department of Electronic Engineering
University of Tor Vergata
Via del Politecnico 1,00133, Rome, Italy

Maria Carla Parrini
Institute Curie, Centre de Recherche
Paris Sciences et Lettres Research University
75005, Paris, France

Elena Loli Piccolomini
Department of Computer Science and Engineering
University of Bologna
Mura Anteo Zamboni 7, Bologna, 40126, Italy

Eugenio Martinelli
Department of Electronic Engineering
University of Tor Vergata
Via del Politecnico 1,00133, Rome, Italy

ABSTRACT

Biological experiments based on organ-on-chips (OOCs) exploit light Time-Lapse Microscopy (TLM) for a direct observation of cell movement that is an observable signature of underlying biological processes. A high spatial resolution is essential to capture cell dynamics and interactions from recorded experiments by TLM. Unfortunately, due to physical and cost limitations, acquiring high resolution videos is not always possible. To overcome the problem, we present here a new deep learning-based algorithm that extends the well-known Deep Image Prior (DIP) to TLM Video Super Resolution without requiring any training. The proposed Recursive Deep Prior Video method introduces some novelties. The weights of the DIP network architecture are initialized for each of the frames according to a new recursive updating rule combined with an efficient early stopping criterion. Moreover, the DIP loss function is penalized by two different Total Variation-based terms. The method has been validated on synthetic, i.e., artificially generated, as well as real videos from OOC experiments related to tumor-immune interaction. The achieved results are compared with several state-of-the-art trained deep learning Super Resolution algorithms showing outstanding performances.

***K*eywords** deep image prior · light time-lapse microscopy · living cell videos · super resolution · convolutional neural networks

1 Introduction

Light Time-Lapse Microscopy (TLM) imaging is successfully used to acquire and record biological experiments based on Organ-On-Chip (OOC) platforms, which are miniaturized microfluidic devices mimicking in-vitro complex 3D cellular micro-environments [1], such as cell migration [2] or multi-cellular interaction [3, 4]. After acquisition by TLM, the live cell videos are analyzed by means of sophisticated computerized algorithms with the aim of finding

* *Citation*: **Pasquale Cascarano et al., Recursive Deep Prior Video: a Super Resolution algorithm for Time-Lapse Microscopy of organ-on-chip experiments, DOI: S1361841521001705.**

biological insights embedded within cell motility. The way in which cell move, indeed, has been discovered meaningful to understand biological processes, such as wound healing [5] and morphogenesis [6] but also cancer growth and spread of metastasis [7]. Usually, the automated exploitation of such devices includes the localization and tracking of cells through increasingly cutting-edge single particle tracking software [8, 9, 10, 11]. Cell trajectories are then coded in time and space domain by extracting some motility descriptors useful to uncover and quantitatively evaluate the response to target therapeutic agents [12, 13]. However, the reached biological conclusions can be compromised by the experimental set-up of TLM in terms of spatiotemporal resolution [14, 15]. First of all, a suitably high frame rate is required to entirely capture and then to accurately estimate the duration of biological events such as apoptosis or cell-cell interaction. Not less relevant, a high spatial resolution implies many benefits for the video analysis. Spatial resolution of a light TLM video frame refers to the number of pixels composing the image for a fixed field of view. The higher pixel density, characterizing the so-called High Resolution (HR) images with respect to Low Resolution (LR) ones, reveals to be essential to better distinguish particles within a video and hence to effectively dissect intricate biological phenomena involving multiple cell populations. Multi-cellular interaction may constitute an example: during interaction, the distance among cells reduces until they overlap. A high spatial resolution may decrease cell detection and tracking errors showing more defined and detailed shapes and edges. As a result, a more reliable tracking positively affects the trustworthiness of the motility descriptors extracted from the trajectories thus uncovering unbiased biological findings. Unfortunately, acquiring HR images is not always possible, due to the high cost of the high performing acquisition instruments and physical constraints, such as the optical zoom provided by the camera. However, if a higher magnification is feasible, it does not certainly guarantee a better image clarity. In addition, HR images related to long-term experiments, i.e., from hours to days, can reach a size from tens to hundreds of gigabytes, thus requiring very high processing capabilities. A fair compromise between high computational requirements and the preservation of the biological informative content may be represented by the adoption of Super Resolution (SR) algorithms: experiments can be acquired at a LR and then post-processed by means of SR algorithms. In the classical LR image formation model, the LR data is assumed to be a down-sampled and noisy version of the HR data. By passing from HR to LR image, some high-frequency details are lost, and, as consequence, the inverse process of reconstruction from LR to HR image represents an ill-posed problem, namely, many HR images result to be related to a single LR image. To effectively reconstruct the HR image from the LR one, many of the most efficient SR methods proposed in the literature require a-priori information on the HR data that should be retrieved [16]. Other SR methods utilize deep learning to learn the statistical correlation between LR images and their HR counterparts from an external database of training examples [17, 18, 19, 20]. In the last decades, SR algorithms have been covered a wide spectrum of applications, from medical imaging [21, 22, 23], thermal imaging [24, 25], remote sensing imaging [26], to security imaging [27]. To the best of our knowledge, SR algorithms have been also formulated for fluorescence microscopy applications [28, 21, 29, 30, 31], whereas they have been not developed for light microscopy applications, especially if referred to experiments from OOC devices. In this paper, we propose a novel super resolution framework based on the recently developed Deep Image Prior (DIP) [32] that we apply to light TLM videos representing living cell migration and interaction. We introduce three algorithms: the Deep Prior Video (DPV), which is an extension of DIP to video frames, the Recursive Deep Prior Video (RDPV), based on a recursive updating rule for the weights of the network, and, finally, a regularized version of RDPV based on Total Variation. As well as for the DIP framework, the proposed approaches exploit the prior knowledge on the solution carried by Convolutional Neural Network (CNN) structures. One of the most striking novelty of the proposed methods is that it does not require any training step, being totally unsupervised, thus drastically reducing the time of running and accelerating the experimental response on cell behavior from TLM experiments. Three additional main novelties are introduced. Firstly, a sharing parameters-based technique among consecutive video frames is implemented: RDPV takes in input one frame of a TLM video at a time and uses the knowledge of previous super resolved video frames to reconstruct the new one through a new recursive updating rule for the weights of the network. Secondly, a stopping rule is fixed to reduce the running time and avoid overfitting, which is typical in the classical DIP framework. Finally, inspired by [33], we boost the performances of the RDPV by adding two commonly used Total Variation (TV) terms, namely isotropic TV (RDPV-TVi) and anisotropic TV (RPV-TVa) [34]. In Fig. 1 an example of video frame reconstruction with RDPV is shown. The favorable effect of super resolution on cell localization, edge map detection and cell tracking is also highlighted. The application of the RDPV algorithm allows us to reduce the false occurrences during the cell localization phase (Cell localization in Fig. 1), to successfully separate cells in contact (Edge detector in Fig. 1) and to effectively construct cell trajectories (Cell tracking in Fig. 1). The proposed DPV, RDPV and its TV-based variants are validated on synthetic videos, i.e., artificially generated, and real videos from organ-on-chip experiments. As results, RDPV and its regularized versions greatly improve the performances obtained by the application of the classical DIP approach on videos, DPV. The new methods are also compared with the state-of-the-art of trained deep learning-based SR algorithms, achieving very promising results [17, 18, 19, 20]. The evaluation of the super resolved image quality improvement is performed by using classical metrics such as Peak-Signal-to-Noise-Ratio (PSNR) and the Structural Similarity Index Measure (SSIM) [35]. In addition, the connection between the reliability of the biological information and the spatial resolution of the live cell videos is assessed.

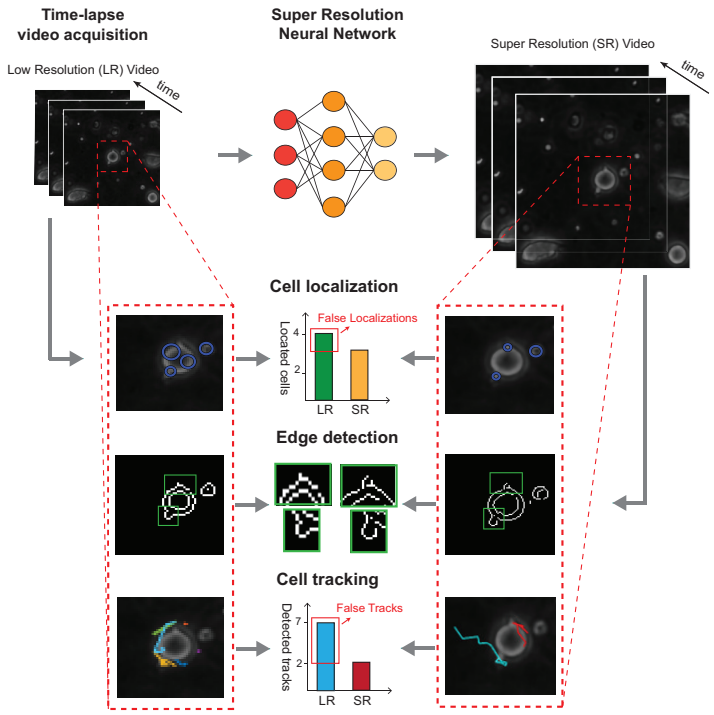

Figure 1: **More effective cell motility evaluation moving from Lower Resolution to Super Resolution videos.** The number of false occurrences during the cell localization phase is reduced (Cell localization); cells in contact are separated thanks to an efficient edge detection (Edge detector); cell trajectories are effectively constructed (Cell tracking).

2 A Brief Survey on Super Resolution

In the field of Super Resolution, the Single Image Super Resolution (SISR) task, which is the problem of reconstructing an HR image from a single LR image, has mostly caught the attention among the researchers. In the discrete setting, the SISR observation model can be fixed as follows:

$$Sx + \eta = y, \tag{1}$$

where $S \in \mathbb{R}^{NM \times L^2 NM}$ is the degradation matrix which links the HR image $x \in \mathbb{R}^{L^2 MN \times 1}$ to the LR image $y \in \mathbb{R}^{MN \times 1}$, both reshaped as vectors. In particular, N and M are the width and the height of the LR data, respectively, whereas the positive integer L, also known as magnification factor, is the square root of the ratio between HR and LR images dimensions. Moreover, $\eta \in \mathbb{R}^{MN \times 1}$ is the Additive White Gaussian Noise (AWGN) component of standard deviation σ, which corrupts the LR measurement. Mathematically, the SISR problem is known to be strongly ill-posed [16], therefore its solution turns out to be sensitive to the presence of noise in y. Moreover, the linear system in (1) is an underdetermined system, i.e., many HR images are related to the acquired LR image y; hence, inverting the process described by (1) does not lead to a unique solution. In the literature, many approaches have been proposed in order to get a good estimate of x. Among them, the interpolation-based methods reallocate the LR image pixels on a finer grid, then the missing pixel values are estimated using interpolation techniques such as Bicubic interpolation and Lanczos resampling [36]. Even if the interpolation-based methods are computationally cheap, they suffer from accuracy issues since they are not capable to retrieve the missing high frequency details. Another common approach in the literature is to shrink the space of the possible solutions by exploiting some prior knowledge on the desired solution. This is done in different ways by the algorithms belonging to the class of reconstruction-based SISR and learning-based SISR methods, which are currently the state-of-the-art. The reconstruction-based methods rewrite the problem (1) as the following unconstrained minimization problem:

$$x^* \in \underset{x}{\operatorname{argmin}} \, \|y - Sx\|_2^2 + \lambda \rho(x). \tag{2}$$

The objective function in (2) encodes both the information on the fixed observation model (type of noise, blur, downsampling, etc.) and the prior information on the solution (smoothess, sparsity, etc.) through the first and the second

term of the sum, respectively. The scalar parameter λ is an hyperparameter which represents a trade-off between the two terms [16]. Despite their good performances, their flexibility and their strong mathematical foundations, the quality of the reconstruction computed by these methods degrades rapidly when the magnification factor L increases.
Learning-based SISR methods utilize Deep Neural Network (DNN) architectures to learn the statistical correlation between the LR and the HR image in a supervised framework given a training set of examples. They attempt to solve the following minimization problem:

$$\theta^* \in \underset{\theta}{\operatorname{argmin}} \mathcal{L}(f_\theta(y), x) \quad \text{for } y \in Y, x \in X, \tag{3}$$

where f_θ is a fixed DNN architecture with weights θ, $\mathcal{L}$ is a loss function, and $\{(y, x)\}_{y \in Y, x \in X}$ is a large given set of LR and HR example pairs. Then, for a generic LR image $\tilde{y}$, the HR reconstruction $\tilde{x}$ is obtained as $\tilde{x} = f_{\theta^*}(\tilde{y})$. The success of supervised learning-based methods is due to the capacity of these models to handle a big amount of data and capture image statistics. Among the more powerful deep learning methods for SISR, we mention the Enhanced Deep Super Resolution (EDSR) neural network [17], and the Residual Channel Attention Network (RCAN) [18], both based on CNN structures, and the Enhanced Super Resolution Generative Adversarial Networks (ESRGAN) [20] which exploits an adversarial training. However, their outstanding performances require a varied set of examples and consequently an overstated computational effort. Moreover, in most cases, the trained deep architectures are specialized for a fixed magnification factor L, requiring to repeat the training if a different magnification factor is needed. It is worth saying that is quite difficult in real applications either to acquire images of the same scene with different resolutions or dispose of a varied data set. In addition, these methods can exhibit instability issues due to the presence of unseen degradation patterns like blurring, additive noise and compression artifacts affecting the LR data [37].
Super Resolution techniques have also been developed to enhance the spatial resolution of videos by exploiting inter-frame information among succeeding LR frames. The most efficient real-world Video Super Resolution (VSR) methods rely on motion estimation and motion compensation (MEMC), that are common strategies for aligning neighbouring frames. However, MEMC techniques can fail when the lighting changes drastically, the objects captured in the field-of-view (FOV) appear out-of-focus or great motions occur along succeeding LR video frames [37, 38]. Therefore, VSR approaches are usually applied to videos with high-temporal acquisition frequency, i.e., from 15 to 60 frames per second, or acquired at a lower frame-rate with sub-pixel motions among neighbouring frames [37, 38]. In contrast to the MEMC-based VSR methods, Recurrent Convolutional Neural Network (RCNN) based approaches [37, 38] exploit Recurrent Neural Networks to extract spatial and temporal information directly from the LR frames. In general, Recurrent Neural Networks are difficult to train and sometimes suffer from the gradient vanishing problem. Moreover, they do not provide stable performances and the computational burden limits their implementation on hardware [38]. In this work, we focus on TLM videos of OCC experiments whose LR frames are acquired at fixed frame-rate, from seconds [14] to minutes [9], while containing stationary and dynamic objects, that are tumor and immune cells, respectively. In particular, the immune cells are the main objects of interest of TLM video analysis and are characterized by a high motility (more than 10 pixels shift among consecutive frames), which can also entail they suddenly go out-of-focus (Fig. S1). Therefore, the low frame-rate, the high motility of the immune cells and their sudden out-of-focus behaviour have motivated us to refer to SISR methods applied frame by frame as fair competitors.

3 Method

3.1 Deep Image Prior

In the field of SISR, the difficulty of constructing a set of LR-HR image pairs has prompted researchers to inspect unsupervised learning-based approaches. One of the most interesting works in this direction is Deep Image Prior (DIP) [32]. In their pioneering work, the authors prove that a CNN structure is capable to capture the image features without employing any training set. Indeed, it has been empirically shown that natural images are more easily reproducible than random noise by a deep CNN. The DIP framework is a combination of the following optimization problem:

$$\underset{\theta}{\operatorname{argmin}} \|y - S f_\theta(z)\|_2^2 \tag{4}$$

and a stopping rule (maximum number of iterations), where f_θ is a fixed CNN generator with weights θ, and z is a vector of arbitrary dimensions sampled from a multivariate random variable uniformly distributed. Then, given θ^*, computed by truncating the iterations of standard gradient-based optimization schemes applied to (4), the estimated HR image x^* is computed as $x^* = f_{\theta^*}(z)$. From a theoretical point of view, Ulyanov et al. have shown that, in the first iterates of the involved optimization process, the architecture of a CNN can provide a prior on the solution by reproducing HR noise-free images. Therefore, it is well-known that the choice of the maximum number of iterations is crucial to not reproduce the noise affecting the initial LR data y in the solution x^* [32].
So far, DIP has shown comparable performances with respect to other supervised learning-based methods in the field of

SISR; however, it has some drawbacks that must be solved, e.g., a suitable early stopping rule for the iterative process is needed and the choice of a proper CNN architecture must be accounted.

3.2 Proposed methods

Motivated by the interesting properties of DIP in the SISR field, we make use of this unsupervised learning-based technique to increase the spatial resolution of TLM videos. The used network is an Encoder-Decoder CNN architecture with long skip connections implemented via concatenation [32]. The encoder and decoder parts are made up of four encoder and decoder base units, respectively. The encoder base units accomplish convolutions with 128 features maps, batch-normalization layers and Leaky Relu activations. The downsampling is performed by the convolutional layers setting the stride equal to two. The decoder base units consider again convolutions with 132 features maps, batch-normalization layers and Leaky Relu activations and, in addition, an up-sampling Lanczos operator is introduced. The long skip connections by concatenation added between the encoder and the decoder base units make use of convolutions with 4 feature maps and batch normalization. The architecture and the transformations involved are sketched in Fig. 2.

We now explain in detail the proposed methods and their main features. All of them are applied on one video frame at a time. The input requirements are the LR frames, a fixed random image z having the same spatial size of the unknown HR target x, and the CNN architecture properly initialized. We point out that for all the implemented methods, the whole process reconstructing each HR frame can be divided in two steps: the initialization and the computation steps. The initialization step defines the starting set of weights initializing the fixed CNN architecture. The computation step involves the iterative process solving an optimization problem, such as (4) and its variants, by means of standard iterative gradient-based algorithms. As suggested by [32], we use the ADAM iterative scheme [39]. We give more details in subsection 4.5. As for the standard DIP framework, the iterative process involved requires a stopping criterion. Therefore, for each method, we specify the stopping rule implemented.

We refer to our first proposal as DPV algorithm. This method treats the frames constituting the TLM videos as uncorrelated images initializing randomly the fixed CNN architecture. The computation step solves the optimization problem (4), and, as stopping criterion, a maximum number of iterations is fixed. We remark that DPV can be seen as a simple generalization of the standard DIP to the case of videos.

Our second proposal is the RDPV method. A scheme of the RDPV is depicted in Fig. 3. It differs from the previous DPV algorithm both in the initialization and the computation phase. In order to exploit the correlations among neighboring frames, the fixed Encoder-Decoder with skip concatenations architecture applied to the frame at time $t+1$ is initialized by the set of weights θ^* computed during the computation phase related to the frame at time t. The computation step, depicted in Fig. 3 (green square), differs from the DPV, since the iterative process optimizing (4) is early-stopped by means of an adaptive criterion, which looks at a sliding window of a fixed size including the values of the objective function computed along the iterations. The iterative process ends when these values flatten (for more details *see* subsection 4.5). These novelties lead to better results in terms of quality and computational cost saving with respect to the DPV method.

Our third proposal is inspired by the classical reconstruction-based approach (2). We add to the objective function in (4), the Total Variation priors [34] of the form:

$$\mathrm{TV}_p(u) = \sum_{i=1}^{n} \left(|(D_h u)_i|^p + |(D_v u)_i|^p\right)^{1/p}, \tag{5}$$

where u is a generic 2D image, n is the number of pixels, and D_h, D_v are the first order finite difference discrete operators along the horizontal and vertical axes, respectively. Hence, our third proposal attempts to solve in the computation step the optimization problem:

$$\underset{\theta}{\operatorname{argmin}} \, \|y - S f_\theta(z)\|_2^2 + \lambda \mathrm{TV}_p(f_\theta(z)). \tag{6}$$

The parameter λ is a positive hand-tuned parameter which represents a trade-off between the quadratic term and the TV_p regularizer. By setting $p = 1$ or $p = 2$ in (5), the anisotropic and the isotropic TV are obtained, respectively. Both are usually employed in SR to suppress noisy components and reconstruct HR images with sharp edges [16]. The anisotropic regularizer splits the contribution of the gradient components, whereas they are jointly involved in the isotropic one.
In [33] the authors use the anisotropic TV, while we also consider the isotropic formulation.
The proposed approaches exploit the TV regularizers in order to improve the performances obtained by the standard

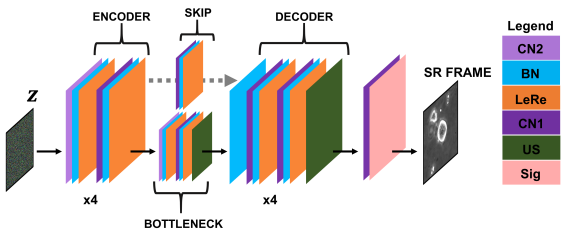

Figure 2: **Encoder-Decoder architecture with long skip connections.** In the legend on the right: CN2 stands for Convolutional layer with stride 2, BN for batch normalization, LeRe for Leaky ReLu activation, CN1 for Convolutional layer with stride 1, US for Lanczos Upsampling, Sig for sigmoid activation. The image z is the random input image of the RDPV method and the SR frame is the computed output.

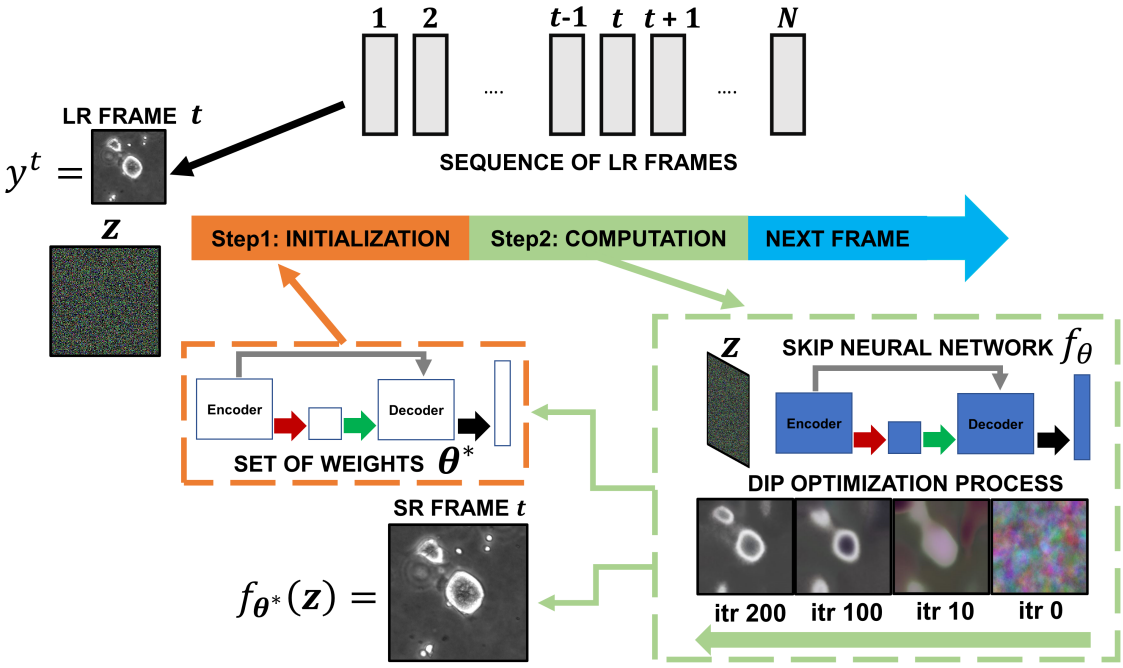

Figure 3: **RDPV scheme.** The input of the proposed RDPV are the sequence of TLM video frames, the random input image z, and the neural network architecture f_θ. The method is divided in two steps: the initialization (orange) and the computation (green) step. At time t, given the input frame y^t, the neural network f_θ is initialized by the set of weights, which are the output of the computation step at time $t-1$. Then, the classical DIP iterative optimization process is carried out until the considered early stopping rule is satisfied. The output of the computation step are the set of weights θ^*, which are used for the initialization of f_θ at time $t+1$, and the SR frame at time t computed as $f_{\theta^*}(z)$.

RDPV. We refer to the methods solving (6) with $p = 1$ and $p = 2$ as RDPV-TVa and RDPV-TVi, respectively. We remark that RDPV-TVa and RDPV-TVi differ from RDPV only in the computation step.

It is worth saying that all the proposed methods are unsupervised since they do not require any training set. We point out that DPV has been considered in order to underline the benefits carried out by the novelties in RDPV and its TV-based variants.

4 Materials and Data Analysis

4.1 Synthetic Cell videos

The dataset of synthetic videos analyzed in the present paper is based on the work by [14], where the authors derive a stochastic particle model to artificially mimic the migration of immune cells towards a target tumor cell and their consequent interaction [40]. Immune cells are considered as single entities which migrate according to a random walk

with drift, constant in modulus. However, at the same time, they interact among them and with a target tumor cell. The tumor-immune interaction is modelled as a repulsive-attractive potential [41] acting for a priori set time, known as effectiveness time. The values of the drift modulus and the effectiveness time are chosen in accordance with estimations from real experiments [40]. A total amount of 100 synthetic videos is generated using MATLAB R2017b (MathWorks, Natick, MA). Each video represents a region of interest of 288×288 pixels containing 16 immune cells and one target tumor cell. A total number of 100 frames is collected for each video emulating a video frame acquisition of 20 seconds. The theoretical trajectories of the total 1600 immune cells (16 for each of the 100 synthetic videos), obtained as result of the implementation of the stochastic particle model, are here considered as ground truth trajectories (GT trajectories). In the following, we will refer to the described atlas of videos as original or noise-free synthetic videos or simply as synthetic videos. The original videos are further corrupted by adding white Gaussian noise with standard deviation $\sigma = 0.001$. In the following, we will refer to the latter videos as corrupted synthetic videos.

4.2 Real Cell Videos

The proposed approach is validated on two sets of real cell videos, namely Videos Type 1 and Videos Type 2, each one containing 10 videos, respectively. They refer to experiments described in a paper by [9], where 3D co-cultures in microfluidic devices embedding 4 cell populations (cancer, immune, fibroblasts, and endothelial) recreate ex vivo a human tumor ecosystem (HER2+ breast cancer). For both video sets, the drug was Trastuzumab (Herceptin, Roche) at 10 mg/mL concentration. Both video sets include untreated control conditions (5 videos) and drug-treated conditions (5 videos). For the Videos Type 1, the two conditions, untreated and drug-treated, are run in parallel, in two different microfluidic devices. The drug is added in the culture medium. Images are taken in parallel using multi-positioning acquisition mode. For the Videos Type 2, the two conditions, untreated and drug-treated, are run sequentially, in the same microfluidic device. The drug is injected inside the microfluidic device by a syringe pump (1 ml/min flow during 1.5 hrs). Videos are acquired before (untreated condition) and after injection (drug-treated condition). Each video represents a Region of Interest (ROI) of 288×288 pixels with a tumor cell occupying its center. Each video frame has been acquired every two minutes. Videos Type 1 count 31 frame, while Videos Type 2 are composed by 57 frames.

4.3 Cell tracking

To the aim of this work, we track cells within the live cell videos under study using the proprietary tracking tool *Cell Hunter* [8, 13, 14], which basically consists of two main stages. First, a localization/segmentation of the cell candidates using the Circular Hough Transform (CHT) [42] allows to estimate cell centers and radii. Among various localization approaches, the CHT has been preferred due to its capability to brilliantly solve the problem of cell occlusion (due to projection errors for example of the 3D scene in the 2D domain) and to properly work in presence of very small objects (immune cells can be represented by a very low amount of pixels). Second, cell trajectories are constructed by linking cell nuclei centers detected along the video frames thanks to an enhanced version of Munkres' algorithm [43] for Optimal sub pattern Assignment Problems (OAP).

4.4 Statistical Analysis

A two-fold evaluation process is carried on. Both synthetic and real videos are involved in a test to verify image similarity between original HR and reconstructed SR video frames based on the computation of two metrics: PSNR and SSIM. For both synthetic and real videos, the average PSNR and the average SSIM values computed over all the video frames are calculated. Since real videos are acquired by inverted microscopes (*see* subsection 4.3), they are affected by undesired effects, e.g., additive noisy patterns, related to external factors or intrinsic limitations of the acquisition instrument [44]. Under this consideration, we filter the acquired frames with a smoothing Gaussian kernel and treat them as ground truth [45]. The PSNR is usually defined in the logarithmic decibel scale (dB) as follows [35]:

$$\mathrm{PSNR} = 20 \log_{10} \left(\frac{\max(Y) - \min(Y)}{\sqrt{\mathrm{MSE}}} \right), \tag{7}$$

where MSE is the averaged square difference between the original HR video frame Y and the super resolved video frame X. The higher the PSNR is, the better the image quality is. Anyway, since such metric is sample-dependent and does not allow predicting the perceived image quality, the perceptual metric SSIM is also used [35]:

$$\mathrm{SSIM} = \frac{(2\mu_X \mu_Y + c_1)(2\sigma_X \sigma_Y + c_2)}{(\mu_X^2 + \mu_Y^2 + c_1)(\sigma_X^2 + \sigma_Y^2 + c_1)}, \tag{8}$$

where $\mu_X, \mu_Y, \sigma_X, \sigma_Y$ are the mean and standard deviation of X and Y, respectively, and $c_i = (max(Y)k_i),\ k_i \ll 1,\ i = 1, 2$ are constants. SSIM takes values in the range $[0, 1]$. The larger the value is, the greater the visual image quality is.

The original synthetic videos are also utilized to evaluate how the performance of the tracking software is affected by the proposed SR algorithms. More specifically, immune cell trajectories detected from the tracking algorithm on LR videos (LR trajectories), on original HR videos (HR trajectories) and on SR videos (SR trajectories) are compared with the theoretical/ground truth trajectories (GT trajectories), i.e., trajectories directly obtained from the implementation of the stochastic particle model in the creation phase of the synthetic videos [14]. This kind of analysis is accomplished only on synthetic videos because theoretical trajectories are not available in real contexts. The tracking algorithm could fail by missing trajectories or by associating tracts corresponding to different detected trajectories to a single ground truth trajectory. For this reason, tracking performances are assessed by computing the percentage of detected cell trajectories with respect to the total number of the ground truth ones and the so-called swapping error [46] that measures the average number of swaps per trajectory.
Two parameters are then drawn out from LR, HR, SR and GT immune cell trajectories: the ensemble-averaged Mean Square Displacement (MSD) [47] and the mean interaction time with the tumor cell [13]. The descriptors extracted from the ground truth trajectories are compared to those extrapolated from LR, HR and SR trajectories. The ensemble-averaged MSD captures the overall diffusive attitude in cell movement and it is expressed as

$$\text{MSD}_t = \langle d(r_i^1, r_i^t)^2 \rangle, \tag{9}$$

where the index i denotes the i^{th} track of length T_i, r_i^t is the position of the i^{th} track at time t, with $t = 1, \ldots, max(T_i)$, d stands for the Euclidean distance, $\langle\rangle$ indicates the mean operator applied to the Euclidean distance. The agreement between pairs of time-continuous MSDs, namely, MSD for GT trajectories *versus* MSD for LR/HR/SR trajectories, is measured by the mutual concordance correlation coefficient (CCC) [48], whose values fall in the range $[-1; 1]$. The greater the CCC value is, the greater the consensus between MSDs is. The other descriptor, i.e., the mean interaction time (MIT) indicates the average number of frames in which each immune cell remains close to the tumor cell, within the interaction radius, defined as twice the sum of tumor and immune cell radii [13, 14]. Pairs of MIT distributions, namely, MIT distribution for GT trajectories *versus* MIT distribution for LR/HR/SR trajectories, are compared using the Student's t-test. We assume that a p-value lower than 0.05 indicates a statistically significant difference between the two distributions under comparison.

Finally, the corrupted synthetic videos are exploited to compare the tracking performances obtained on the SR videos reconstructed by the proposed methods and the competing trained networks. The number of cells detected per frame and the swapping error are computed. The respective MIT distributions are compared with the GT one.

4.5 Simulation Settings

The computation step (*see* subsection 3.2) requires the usage of a gradient-based algorithm to solve either problem (4) or (6), respectively related to the proposed RDPV method and its TV-based variants. In our experiments, we use the ADAM scheme [39] by fixing the learning rate at 10^{-3}. However, through several preliminary experiments, we observe that all the methods provide similar results when the learning rate is chosen in the range $[10^{-4}, 5 \cdot 10^{-3}]$. An automatic early stopping procedure is implemented to avoid overfitting. The core idea is to monitor the objective functions in (4) for the RDPV, and (6) for the RDPV-TVa and the RDPV-TVi to decide when to stop the iterations. This technique considers a window (patience) of consecutive values of the objective function and then, if there is not enough decrease during the iterative process, the algorithms are stopped before the fixed maximum number of iterations is reached.
For the first frame of synthetic videos, we impose a maximum of 1000 iterations with early stopping starting from 500 iterations (patience = 50). For the subsequent frames, due to the initialization step (*see* subsection 3.2), the number of iterations can be reduced: we set a maximum of 500 iterations with early stopping starting from 300 iterations (patience = 50). For the first frame of real videos, we impose a maximum of 3000 iterations with early stopping starting from 2000 iterations (patience = 50). For the subsequent frames the number of iterations is reduced: we set a maximum of 2000 iterations with early stopping starting from 1000 iterations (patience = 50). For a fair comparison, we set the maximum number of iterations for DPV as the number of iterations performed by RDPV according to the aforementioned stopping criterion.
These hyperparameters, i.e., the maximum number of iterations and the starting of the early stopping rule, are chosen in order to provide a fair compromise between reconstruction quality and computational time. Since the best reconstructions are obtained when the loss starts flattening and reaches a steady-state, the starting of the early stopping rule is imposed at about half of the maximum number of iterations. Postponing the starting of the early stopping rule makes the network more prone to over-learn the image statistics also reproducing the noise affecting the LR frame in the SR reconstruction. Moreover, for all the processed synthetic and real frames, the early stopping ends the iterative process before the maximum number of iterations is reached.

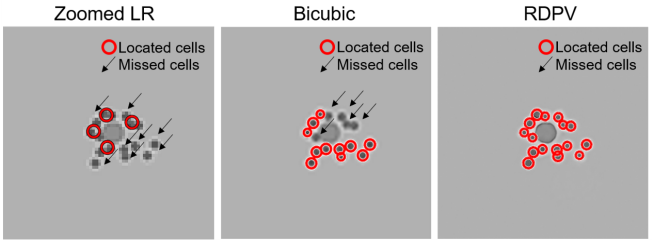

Figure 4: **Immune cell localization on synthetic videos.** Example of cell localization by means of Cell Hunter software on a LR frame (left panel) and the corresponding SR counterparts reconstructed by the Bicubic method (central panel) and the proposed RDPV method (right panel).

Concerning the proposed methods with regularization (RDPV-TVa and RDPV-TVi), we set the trade-off parameter λ in (6) equal to 0.008 for all the reconstructed videos. In our experiments, comparable performances are obtained in terms of PSNR and SSIM if the λ is chosen in the range $[10^{-3}, 10^{-2}]$. However, there are several methods that can be adopted to address the choice of this parameter [49].

All the videos have been downsampled by a factor equal to 4 using the standard Bicubic interpolation and then reconstructed by SR methods setting $L = 4$. Conversely to other lower factors, this choice allows to effectively reduce the spatial burden due to the storage of TLM videos. Moreover, we compare the results achieved by our methods using a magnification factor for which learning-based methods have state-of-the-art results. All the simulations are performed on a PC Intel(R) Core(TM) i7-8700U CPU @ 3.70 GHz 3.70GHz with 32Gb RAM using Python (v3.6.5) and MATLAB R2018b (MathWorks, Natick, MA) on two NVIDIA GeForce GTX 1080 Ti (11 Gb of memory per GPU) boards with CUDA driver (v9.0) and cuDNN library (v7.1.4).

5 Results and discussion

5.1 The importance of super resolution on cell tracking and descriptors extraction

Video analysis usually starts with cell localization and tracking (*see* subsection 4.3). The errors made by tracking algorithms in this phase can propagate and heavily compromise the extrapolated biological conclusions. As demonstrated elsewhere [14], when the spatial resolution is low, the tracking software could fail in its localization task. In order to corroborate this argument, in Fig. 4 we show how the localization algorithm (CHT) acts on LR and SR frames obtained by a coarse SR algorithm and the proposed RDPV, respectively. More precisely, the left panel of Fig. 4 depicts an example of cell localization on the LR synthetic video frame where localized cells are marked as red circles and missed cells are pointed out by black arrows. As a result, we observe that some cells are missed, and others are identified as unique entities because partially overlapped. The most simple and popular choice for image up-sampling is the bicubic interpolation algorithm [50], that is frequently implemented in data analysis software since it quickly provides up-scaled images. In the case of videos, such algorithm is usually applied frame by frame. Despite its rapidity and low computational cost, the bicubic outcome reveals to be blurred with the contour of the cells not sharp. As a consequence, this smoothing effect damages the edge detection of the circular-shaped objects by the CHT. Indeed, as depicted in the central panel of Fig.4, the lack of fine details may lead to inaccurate localization. It is evident how the software is able to distinguish cells but misses some of them. As shown in the right panel of Fig. 4, a more sophisticated SR algorithm, such as the proposed RDPV, allows increasing the trustworthiness of tracking software in localizing cells so that overcoming the limitation of coarse results obtained by the standard bicubic algorithm. This simple test does not only highlight an interesting connection between pixel density and tracking performances, but also the importance of good quality SR reconstructions (*see* subsection 5.4).

The localization algorithm (CHT) provides better performances on higher pixel-density images because it is based on the concept of the accumulation point [42]. Therefore, it is interesting to investigate how the performance of the tracking software and the consequent extraction of some motility and interacting descriptors are affected by super resolved video frames.

A visual comparison between GT, HR, SR, and LR trajectories on synthetic video frames is provided in Fig. 5. A zoom is supplied for a better visualization of the LR trajectories. Conversely to LR trajectories, the appearance of HR and SR trajectories is very similar to that of GT ones. From a quantitative point of view, the percentage of total number of detected LR trajectories on the 100 synthetic videos with respect to the overall number of the GT ones (1600) is equal to 51%, while it reaches the 100% for the detection of both the HR and the SR trajectories. The

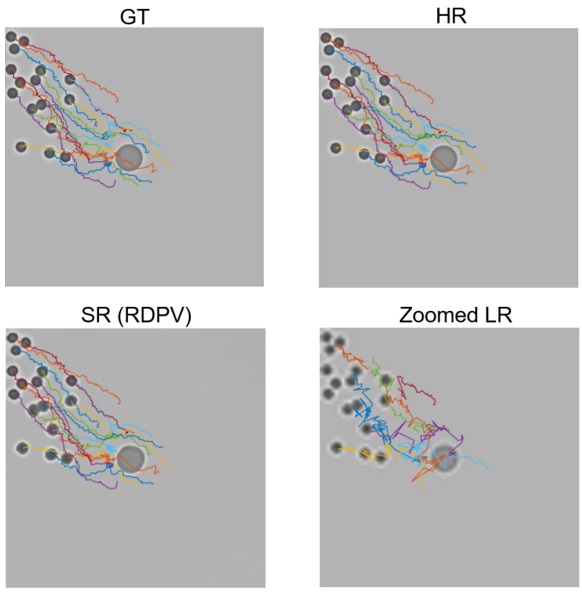

Figure 5: **Visual representation of immune cell trajectories on synthetic videos.** Ground-truth (GT) trajectories directly obtained from the implementation of the model in the creation phase of the synthetic videos (upper-left panel). High resolution (HR) trajectories identified by Cell Hunter software on the original HR video (upper-right panel). Super resolution (SR) trajectories identified by Cell Hunter software on the SR video, reconstructed by the proposed RDPV method (lower-left panel). Lower resolution (LR) trajectories identified by Cell Hunter software on the LR video (lower-right panel). A zoom of LR trajectories is provided for a better visualization (Zoomed LR).

swapping error counts 18.4, 3 and 3.5 swaps per trajectory, for the LR, HR and SR trajectories, respectively. This is a consequence of the previously underlined CHT errors made on LR video frames (Fig. 4), since the estimation of trajectories is strictly correlated to the detection of cells frame by frame. In order to prove that the performance of the tracking software reflects on the consequent feature extraction, we then compare the motility and interaction descriptors (average-ensemble MSD and Mean Interaction Time, MIT) extracted from GT trajectories with those calculated from HR, SR and LR trajectories, respectively. In left panels of Fig. 6, pairs of average-ensemble MSD curves are drawn: the GT curve is juxtaposed on the HR curve in the upper panel, on the LR curve in the central panel, and on the SR curve in the lower panel. The GT and HR curves as well as GT and SR curves are almost completely overlapped producing high CCC values. The LR curve, instead, significantly differs from the GT one resulting in a low CCC value. All the CCC values are highlighted on the respective left panels in Fig. 6. Furthermore, in the right panel of Fig. 6, couple of MIT distributions in comparison are shown: GT and HR distributions in the upper panel, GT and LR distributions in the central panel, and GT and SR distributions in the lower panel. The p-value for the Student's t-test is computed for all the three comparative scenarios. The information carried by HR and SR distributions is reliable (p-values $>$ 0.05), whereas the one related to LR videos is completely biased. The flattening of the LR distribution is an effect of the low spatial resolution: cells are hardly localized and hence the effective number of interacting cells decrease. In this latter case, distributions appear significantly different (p-value < 0.05), despite they represent the same experimental condition. This test confirms that analyzing videos reconstructed by the proposed SR algorithm leads to a minimum information loss with respect to analyzing HR videos and, at the same time, a great information gain with respect to analyze LR videos.

5.2 Image quality evaluation on synthetic cell videos

So far, we have underlined the importance of the high spatial resolution for TLM videos in order to get a successful tracking and extraction of kinematic and interaction descriptors. In Fig. 4, we test the CHT localization algorithm on the SR output of the bicubic algorithm, highlighting that sophisticated SR algorithms are required in order to retrieve fine image details. As exposed in Section 2, some state-of-the-art methods address the problem of SR. To fulfill the task, most of them are based on neural networks and require training on a given dataset. We compare SR videos provided by some of the best performing trained methods, ESRGAN [20], proSRGAN, proSR, proSRs [19], RCAN [18], EDSR [17], all of them applied one frame at time, with those obtained by the proposed non regularized (DPV and RDPV) and regularized (RDPV-TVi) unsupervised learning algorithms. Performances are evaluated on either original or corrupted

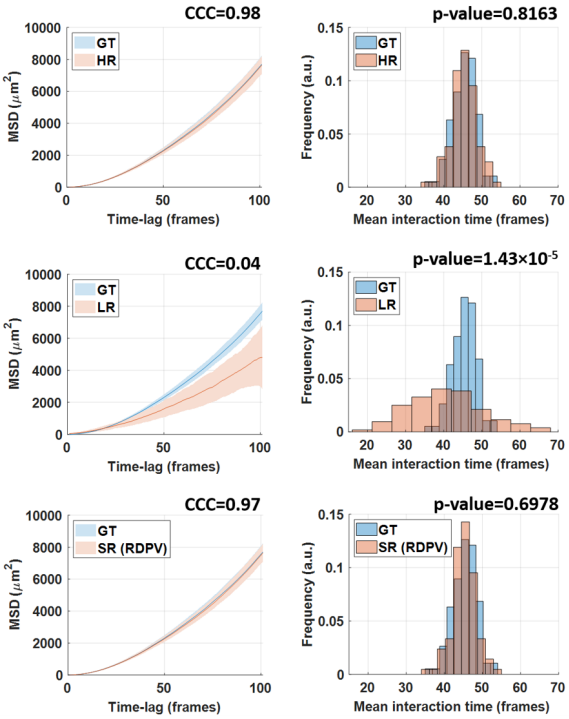

Figure 6: **Performance evaluation in terms of motility and interaction descriptors on synthetic videos.** (left panel) Comparison between couple of Ensemble-Averaged MSD curves: GT vs HR (upper-left), GT vs LR (centre-left), GT vs SR (lower-left). CCC values are also highlighted. (right panel) Comparison between couple of Mean Interaction Time distributions: GT vs HR (upper-right), GT vs LR (centre-right), GT vs SR (lower-right). P-values for the Student's t-test are also indicated. In the legend, GT stands for Ground Truth, HR stands for High Resolution, SR stands for Super Resolution, LR stands for Lower Resolution.

synthetic videos. In Fig. 7, we show the distributions of the average PSNR values computed over all the frames of each of the 100 synthetic videos for all the above mentioned methods. The top panel of Fig. 7 refers to the original synthetic videos, whereas the bottom panel refers to the corrupted synthetic videos. The average SSIM values for each synthetic video are also computed and the relative 95% Confidence Intervals (CIs) are estimated and reported in Table 1: the first column is related to original synthetic videos; the second column is related to the corrupted synthetic videos. The proposed RDPV and RDPV-TVi algorithms always outperform the standard DPV. This is because RDPV implements the new recursive updating rule which takes into account the knowledge acquired by the previous reconstructed frames (*see* subsection 5.3). Moreover, the regularization term within RDPV-TVi adds to the model prior information on the solution that are not completely captured by the fixed CNN architecture. In such a way, we attenuate one of the main flaws of the standard DIP framework, that is the choice of the network architecture. Very promising results are achieved from the comparisons with the trained networks. Comparable performances are observed on noise-free artificial videos (upper panel of Fig. 7). Better performances are achieved on corrupted artificial videos (lower panel of Fig. 7). This is because one of the main drawbacks of trained architecture is the instability with respect to the presence of noise components in the input data [37]. They are not able to filter out the added noise from test images if the training dataset does not present a considerable number of noisy-images at different levels of noise. Anyway, this necessity might be limiting in practical applications. The presented results stress the importance of developing an algorithm whose output is not dependent on a fixed set of image examples. According to such quantitative results, we depict images obtained by the worst and the best trained methods (ESRGAN and RCAN, respectively) alongside GT, LR, DPV, RDPV and RDPV-TVi images. More specifically, Fig. 8 shows a noise-free synthetic video frame, while Fig. 9 highlights one of the video frames for the corrupted synthetic videos. For the noise-free synthetic videos, RCAN achieves the best performance in terms of average PSNR and SSIM but, as emerged from Fig.8, the immune cells shape appears distort (red and green arrows). The same warping also holds for the ESRGAN method. The standard DPV, instead, is not able to guarantee a fine result, conversely to RDPV which, on its part, has the drawback to not effectively separate some of the immune cells (red and green arrows). The addition of TV regularization (RDPV-TVi) leads to optimal results both in terms of immune cell shape and differentiation. For the corrupted synthetic videos in Fig. 9, these remarks are still valid. An example of original synthetic video and the relative LR version are provided by Movies 1-2. The

reconstructed counterpart from all the SR methods are Movies 3-11. An example of corrupted synthetic video and the relative LR version are provided by Movies 13-14. The reconstructed counterpart from all the SR methods are Movies 15-22. Please refer to Supplementary Materials for more details.

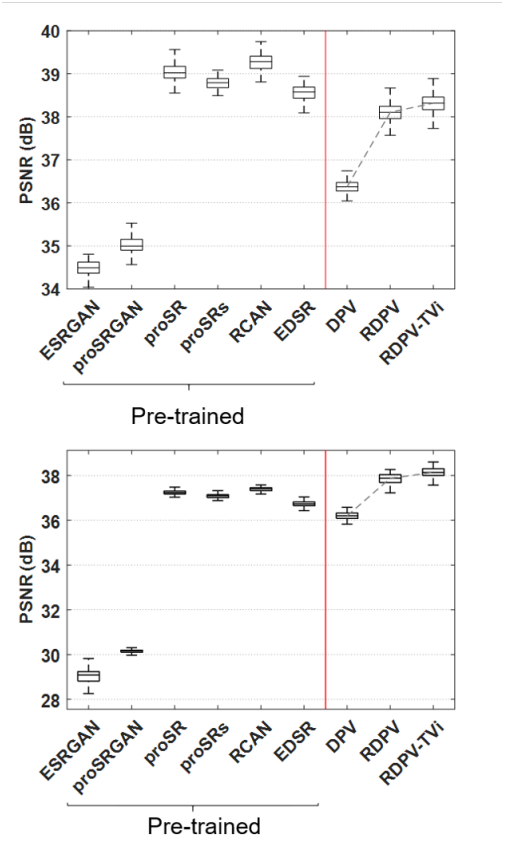

Figure 7: **Quantitative results in terms of PSNR on synthetic videos** ($\sigma = 0$, upper panel) **and their corrupted counterparts** ($\sigma = 0.001$, lower panel). Boxplots comprise the average values of PSNR computed over all the frames of each synthetic video.

Table 1: **Quantitative results in terms of SSIM on synthetic videos** ($\sigma = 0$) **and their corrupted counterparts** ($\sigma = 0.001$)**.** The 95% CI of the average SSIM values computed over all the frames of each synthetic video is reported.

	SSIM (95% **CI)**	
Methods	$\sigma = 0$	$\sigma = 0.001$
ESRGAN	[0.9587, 0.9596]	[0.5748, 0.5814]
proSRGAN	[0.9831, 0.9834]	[0.6733, 0.6752]
proSR	[0.9915, 0.9917]	[0.9552, 0.9553]
proSRs	[0.9923, 0.9924]	[0.9531, 0.9532]
RCAN	[0.9923, 0.9925]	[0.9545, 0.9546]
EDSR	[0.9913, 0.9914]	[0.9548, 0.9549]
DPV	[0.9804, 0.9807]	[0.9763, 0.9768]
RDPV	[0.9904, 0.9907]	[0.9884, 0.9888]
RDPV-TVi	[0.9918, 0.9922]	[0.9915, 0.9917]

5.3 Effect of the recursive updating rule

The proposed methods RDPV and RDPV-TVi outperform DPV in terms of PSNR (*see* Fig. 7) and SSIM (*see* Table 1) either for noise-free or corrupted synthetic videos. The main functioning mechanism of RDPV and RDPV-TVi is the recursive initialization step described in subsection 3.2. The implemented rule is based on the idea that the set of

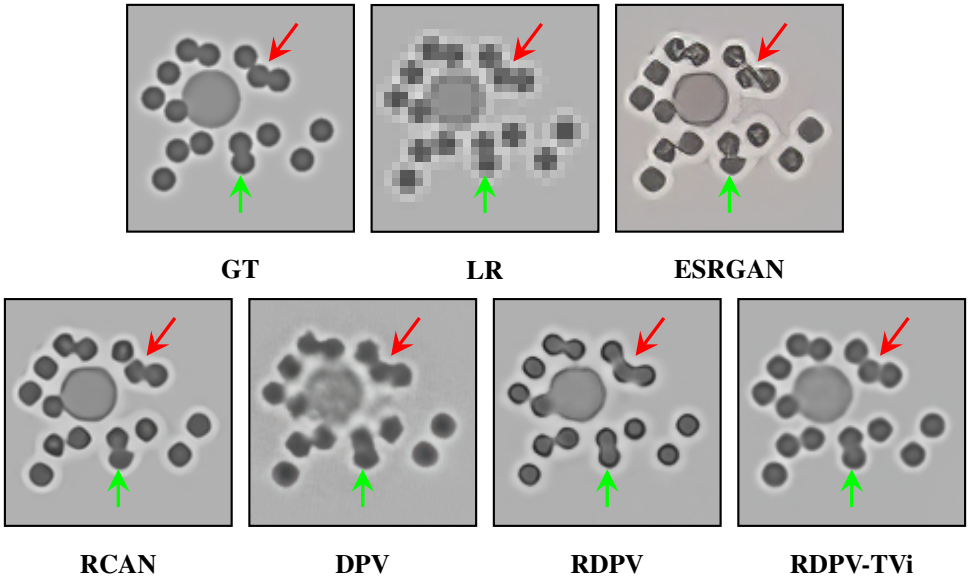

Figure 8: **Synthetic Frame reconstruction close-ups (x2),** $L = 4$**,** $\sigma = 0$**.**

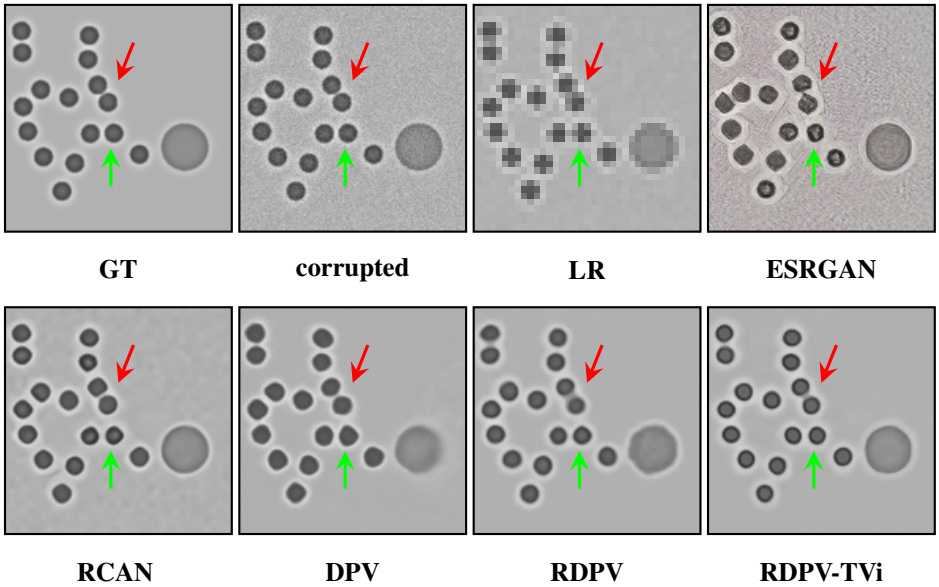

Figure 9: **Synthetic Frame reconstruction close-ups (x2),** $L = 4$**,** $\sigma = 0.001$**.**

weights reproducing a good quality SR frame at time $t + 1$ is not far from the one generating a good quality SR frame at time t, therefore the latter weights can be considered as a coarse approximation of the former ones and then used as starting point in the computation step. To better understand how the implemented rule affects the frames quality along the video, Fig. 10 shows the PSNR values for DPV, RDPV, RDPV-TVi at different increasing timepoints. In the upper and lower panels, the boxplots comprise the average values of PSNR computed over the first two and last two frames of each synthetic video, respectively, where the first two frames refer to the two initial frames exploiting the initialization step. By comparing the two panels, we can observe how the PSNR values of the proposed RDPV and RDPV-TVi increase in the lower panel, whereas those related to DPV remain quite stable. In the central panel, the boxplots depict the average values of PSNR computed over 50 consecutive frames sampled from the middle part of each synthetic video. Two aspects need to be clarified. First, the PSNR values related to DPV has almost the same median at varying timepoints. However, high PSNR values are reached on the first two and last two video frames (upper and lower panels). It may be justified by the fact that at the beginning and at the end of the videos immune cells are migrating

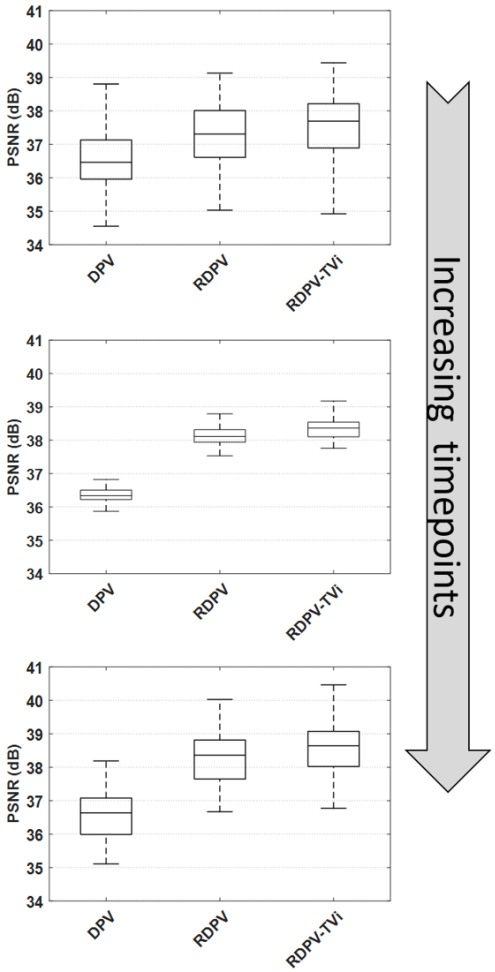

Figure 10: **Effect of the recursive updating rule on image quality in terms of PSNR at different increasing timepoints.** In the upper and lower panels, boxplots comprise the average values of PSNR computed over the first and last two frames of each synthetic video, respectively, where the first two frames refer to the two initial frames whose reconstruction exploits the initialization step. In the central panel, boxplots comprise the average values of PSNR computed over 50 frames at the half of each synthetic video, respectively.

towards and away from the tumor cell, respectively. The cells are more separated and hence their shape and edges are easier to reconstruct. Conversely, in the middle part of the videos, immune cells are interacting with the tumor cells causing overlapping with the tumor cell or among each other. In this last case, the image features are more complex to super resolve since the cells are closer to each other and their edges are not clearly separated. Second, PSNR values related to RDPV and RDPV-TVi are slightly higher than the PSNR values referred to DPV on the first two frames (upper panel of Fig. 10) and progressively increase reaching ever higher values (central and lower panels of Fig. 10). Good performances are also maintained on the half of the videos where immune-tumor interaction occurs. Similar observations remain still valid when we consider SSIM as evaluation metric (Fig. S2). However, we point out that the boxplots in the upper and lower panels of Fig. 10 and Fig. S2 exhibit a higher variance than boxplots in the central panels because the average of the two metrics has been computed on a lower number of frames (two) per video. Finally, these results confirm that the implemented recursive rule positively affects the image quality.

5.4 Connection between image quality and tracking performance

We investigate the connection between image quality and tracking performances on the corrupted synthetic videos, that represent a more realistic and challenging scenario for the application of the tracking software. First, the tracking software is applied on the corrupted synthetic videos reconstructed by all the methods involved in the image quality comparison. Subsequently, the performance of the tracking software is evaluated in terms of explanatory numerical

quantities reported in Table 2. The number of cells detected per frame by means of CHT with sensitivity value of 0.96 as well as the swapping error are calculated, and the respective 95% CI is estimated. The consequent feature extraction is assessed in terms of p-value obtained for the Student's t-test when the GT and SR distributions for the MIT parameter are compared (first column of Table S1). As result, from Table 2, it is evident that the tracking software detects the lowest number of cells per frame and is affected by the highest swapping error when dealing with the reconstructions provided by the less performing pre-trained methods in terms of PSNR (Fig. 7) and SSIM (Table 1), i.e, ESRGAN and proSRGAN. Conversely, the proposed RDPV and RDPV-TVi methods, that achieved the best PSNR and SSIM values in image quality evaluation for the super resolved video frames, are characterized by a slightly higher number of cells detected per frame and a slightly lower swapping error than the other pre-trained methods (*see* Table 2). As explained in the previous subsection, the video frames representing tumor-immune interaction are the hardest frames to reconstruct because cells are really close to each other and partially overlapped. It is interesting to show how the methods used to reconstruct videos can affect the detection of immune cells during the interaction phase. In Fig. S3 we depict the number of immune cells detected on the interaction frames alone that are reconstructed by the proposed methods, RDPV and RDPV-TVi, and the best and the worst pre-trained methods, ESRGAN and RCAN, respectively. The distributions of the number of interacting cells are approximated by normal distributions. The maximum number of cells that are admitted to be detected is 16 and is highlighted by a vertical red line. We observe that RDPV-TVi and ESRGAN provide the curves-fitting with the highest and the lowest mean value, respectively, whereas RDPV shows a comparable distribution with respect to RCAN. It is also interesting to observe how the poor performance of the tracking software on videos reconstructed by ESRGAN and proSRGAN badly affects feature extraction, namely, the computation of MIT parameter, leading to a bias in the interpretation of the results (first column of Table S1). Indeed, for both methods, the p-values for the Student's t-test shows a non-existent statistically significant difference between the SR and GT distributions (p-values < 0.05). Instead, no statistically significant difference is recognized for all the other methods (p-values > 0.05). These results are obtained by imposing a sensitivity value equal to 0.96 as input of the Matlab function *imfindcircles* that implements CHT. Sensitivity values controls the number of circular objects that can be identified: higher values make possible to increase the number of detected objects also recognizing weak and partially obscured circles, but can increase the detection of false occurrences. For a higher sensitivity values, such 0.98, also used to calculate the tracking performance in the subsection 5.1, the number of detected cells per frame and the swapping error for all the compared methods (Table S2) are quite comparable. However, the method RDPV-TVi continues to overcome the other methods and the pre-trained methods ESRGAN and proSRGAN show the lowest performances. In addition, all the methods exhibit a p-value greater than 0.05 (second column of Table S1). Finally, from our investigation, the tracking performance and the image quality of the reconstructed video frames reveal to be strictly related, especially when a crucial parameter for the tracking software, such as sensitivity, is not tuned as optimal as possible. In order to obtain reliable biological conclusions, the importance to combine high quality images and ad-hoc parameter setting also emerges. However, since tuning parameter can be an expensive process, a stable method with respect to parameter setting can be preferred: according to the presented results, RDPV and RDPV-TVi are quite stable methods with respect to sensitivity parameter.

Table 2: **Comparison among the tracking performance on the corrupted synthetic videos super resolved by the proposed and the competing methods.** The tracking performance is evaluated in terms of the number of the cells detected per frame (first column) and the swapping error (second column) by computing the respective 95% CIs.

Methods	Num. cells per frame	Swapping error
ESRGAN	[10.3, 10.4]	[12.1, 12.9]
proSRGAN	[9.7, 9.8]	[13.3, 14.1]
proSR	[12.1, 12.2]	[6.4, 6.9]
proSRs	[11.8, 11.9]	[6.5, 7.0]
RCAN	[12.6, 12.7]	[5.9, 6.4]
EDSR	[11.2, 11.3]	[7.7, 8.3]
DPV	[11.9, 12.1]	[6.2, 6.6]
RDPV	[13.2, 13.3]	[5.0, 5.4]
RDPV-TVi	[14.0, 14.1]	[4.1, 4.5]

5.5 Image quality evaluation on real cell videos

We finally validate the proposed approach on videos from two diverse OOC experiments by exploiting tumor-immune interaction: Videos Type 1 and Videos Type 2. For details about videos, please refer to Section 4.2. As for the synthetic videos, we compare the quality of ground truth frames with those achieved by the proposed methods, without and with regularization, i.e., DPV, RDPV and RDPV-TVi/RDPV-TVa, respectively, also including the trained methods.

Table 3: **Quantitative results in terms of SSIM on real Videos Type 1 and on real Videos Type 2.** The 95% CI of the average SSIM values computed over all the frames of each real video is highlighted.

	SSIM (95% CI)	
Method	Videos Type1	Videos Type2
ESRGAN	[0.8444, 0.8743]	[0.8707, 0.8843]
proSRGAN	[0.9240, 0.9383]	[0.9172, 0.9314]
proSR	[0.9731, 0.9769]	[0.9767, 0.9789]
proSRs	[0.9716, 0.9756]	[0.9749, 0.9770]
RCAN	[0.9741, 0.9777]	[0.9773, 0.9793]
EDSR	[0.9715, 0.9756]	[0.9758, 0.9777]
DPV	[0.9436, 0.9488]	[0.9295, 0.9417]
RDPV	[0.9582, 0.9654]	[0.9548, 0.9608]
RDPV-TVa	[0.9681, 0.9722]	[0.9653, 0.9694]
RDPV-TVi	[0.9686, 0.9723]	[0.9653, 0.9685]

In the upper and lower panels of Fig. 11, we show the average PSNR values for Video Type 1 and Video Type 2, respectively. The first and the second columns of Table 3 report the 95% CI of the average SSIM values for Video Type 1 and Video Type 2, respectively. The average PSNR and SSIM values are computed over all the frames of each of the real videos of the two types. An example of Video Type 1 and the relative LR version are provided by Movies 23-24. The reconstructed counterpart from all the SR methods are Movies 25-34. An example of Video 2 and the relative LR version are provided by Movies 35-36. The reconstructed counterpart from all the SR methods are Movies 37-46. Please refer to Supplementary Materials for more details. The proposed methods RDPV,RDPV-TVi and RDPV-TVa outperform the standard DPV both for Video Type 1 and Video Type 2 in terms of average PSNR and SSIM. We stress that the addition of both isotropic and anisotropic Total Variation improve the performances of the RDPV, confirming once again the importance of these additional terms. For what concerns the comparisons with the trained architecture, RDPV, RDPV-TVi and RDPV-TVa outperform them in terms of average PSNR on Video Type 1 (top panel of Fig. 11) and reach comparable performances on Video Type 2 (bottom panel of Fig. 11). According to the SSIM metric, the proposed methods, RDPV, RDPV-TVi and RDPV-TVa, reach slightly lower performances with respect to the best trained algorithms (Table 3).

Not less relevant, from the PSNR distributions shown in the boxplots in Fig. 11, it is remarkable to see that the distributions of the average PSNR values have a high variance whereas unsupervised methods have more stationary performances over all the tests executed on real videos. This is more evident for the average PSNR distributions on Video Type 1 (top panel of Fig. 11). This highlights a stronger sensitivity to the given input frames for the trained methods with respect to the unsupervised ones. We stress that, for each of the two video types, even if the frames recorded belong to the same experiment, some conditions may change from one video (or even frames) to another, such as the brightness of the FOV. Indeed, analyzing the acquired videos, we observe that sudden changes of luminosity are evident especially for Videos Type 1 (*see* Movie 23), thus negatively affecting the performances of trained methods in some cases. This confirms the need of unsupervised methods for TLM videos super resolution, since it not feasible to collect a dataset accounting all the possible real boundary conditions.

As qualitative evaluation, in Fig. 12 we depict a video frame example (from Videos Type 2) obtained by the worst and the best trained methods (ESRGAN and RCAN, respectively) alongside GT, LR, DPV, RDPV and RDPV-TVi images. For a better visualization of the edges of the portrayed cells, Fig. 13 shows the edge map of the same video frame example after applying Canny Filter [51]. In both Fig. 12 and 13, three regions of interest are closed-up and highlighted by using three different coloured squares: red, green and blue. All the approaches increase the resolution of the starting LR frame and in particular all of them are able to separate the cells belonging to the cluster within the red square. However, as it is evident from the edge map (Fig. 13, red square), the trained approaches introduce artifacts alongside the cell cluster. Such artifacts can dramatically affect the cell tracking software in the localization phase thus identifying false positive cell candidates. We observe that all the unsupervised methods reach quite similar results with respect to the ground-truth image. However, the cells within the cluster (Fig. 13, red square) look better separated for the image obtained by RDPV-TVi, thus confirming that the addition of the Total Variation regularizer improves the results.

5.6 Cell Tracking on SR real videos

We have previously carried on a detailed analysis on synthetic videos showing the importance and the efficiency of our method used as preprocessing step on their low resolution counterparts before tracking and feature extraction are performed. We now test the tracking software on the SR Video Type 1, obtained using the RDPV-TVi method, and on

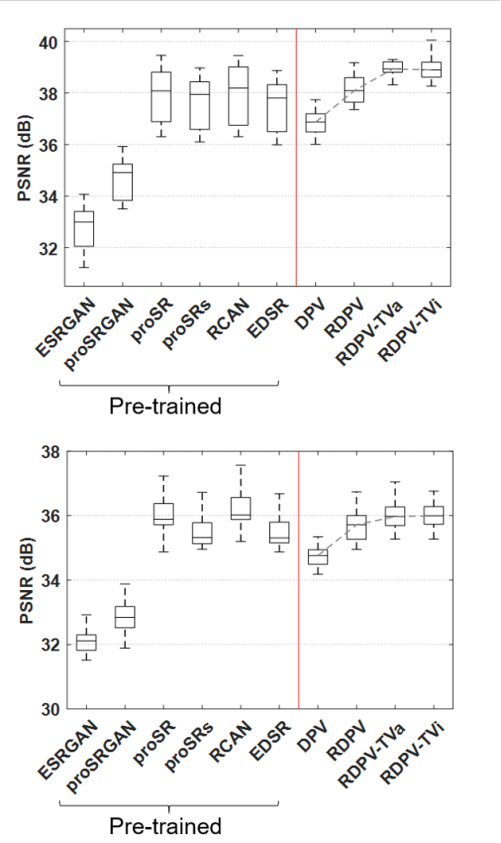

Figure 11: **Quantitative results in terms of PSNR on real Videos Type 1 (upper panel) and Type 2 (lower panel).** Boxplots comprise the average values of PSNR computed over all the frames of each real video.

its LR counterpart. Unfortunately, in this case the ground truth trajectories are not available, since this is a real video and not a simulated one. In Fig. 14, we compare the LR trajectories with the SR trajectories. The frame is a part of a real video in which two immune cells interact with a tumor cell. In the right upper corner of Fig. 14, the trajectories detected on the starting low resolution video are represented. As we can observe, the tracking software assigns more than two trajectories to the immune cells for a total of 7 trajectories, which appear, moreover, very segmented and unrealistic. Conversely, giving to the tracking software the SR video computed using the RDPV-TVi method only two trajectories are detected, thus resulting more realistic.

5.7 Comparison with a learning method trained on a dataset of cell images

To conclude the discussion related to real videos, we want to evaluate how the performance of the most performing trained network, RCAN, varies with respect to the training set employed. More specifically, since RCAN weights are taken as in the pre-trained model available online [2], the question is whether training RCAN on cell images and on images with similar patterns leads to an improvement of the performances. To adequately address the question, by following the same protocol expressed in [18], we train the RCAN architecture on two new datasets: the first one composed by some frames of the synthetic videos and Videos Type 2; the second one composed by some frames of the synthetic videos and Videos Type 1. We trained the same architecture of the original RCAN proposed by [18]. We also investigate if RCAN parameters, e.g., learning rate and batch-size, could be optimized for the task under study. Concerning the learning rate, we use the exponential decay rule implemented in Python Tensorflow, as also suggested in [18], that effectively reduces the running loss during the training phase. Finally, we choose a batch size equal to 16, that is the greatest value our simulation device is able to handle without storage issues. We test the trained architecture that we call tRCAN on the real videos not considered in the training: Videos Type 1 for the first case, Videos Type 2 in the second case. We also compare the achieved performances with those of the DPV, RDPV, RDPV-TVi and RDPV-TVa methods. In Fig. 15, we report the comparison in terms of average PSNR computed on each of the 10 Videos Type

[2] https://github.com/yulunzhang/RCAN

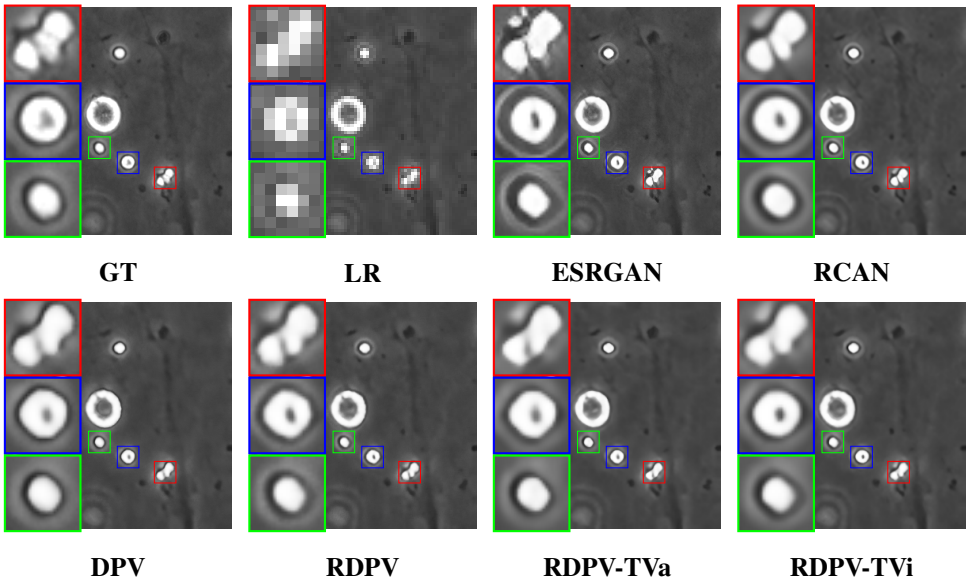

Figure 12: **Real Frame of Videos Type 2,** $L = 4$.Three regions of interest are also closed-up and highlighted by blue, green and red squares.

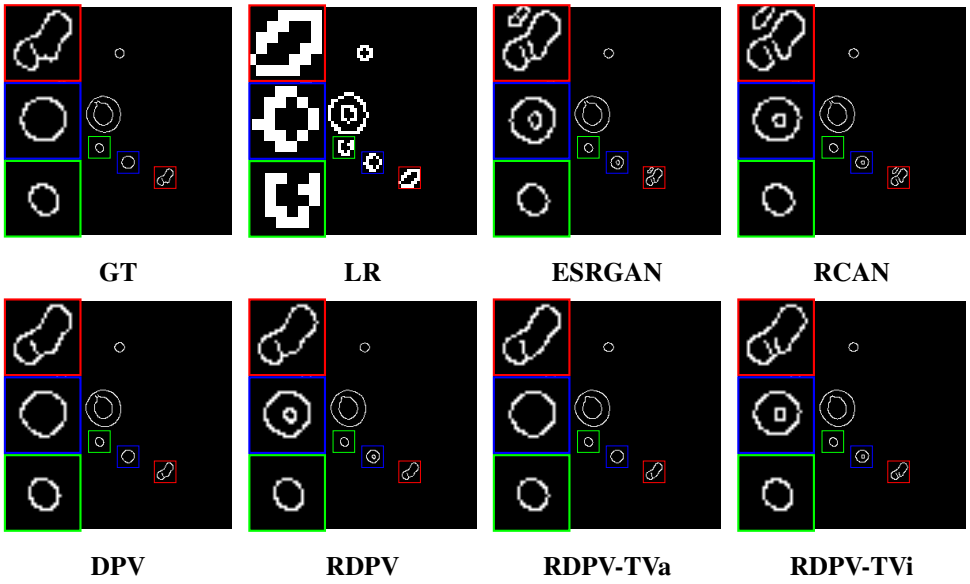

Figure 13: **Real Frame of Videos Type 2,** $L = 4$**, Canny images.** Three regions of interest are also closed-up and highlighted by blue, green and red squares.

1 (upper panel) and on each of the 10 Videos Type 2 (lower panel). By comparing the boxplots related to tRCAN in Fig. 15 with those referred to RCAN in Fig. 11, the usage of a new training set made up of cell images reduces the variance of the average PSNR distributions, thus confirming that the output of the supervised method RCAN is strictly related to the given dataset. The two PSNR distributions do not exhibit a significant increase of the median values. However, a significant improvement is related to the lowest values of the distributions. In order to further enhance the performances of the RCAN, we should add more cell frames belonging to a wide range of real-world experiments, thus resulting not feasible for real applications. As shown in Fig. 15, the proposed methods RDPV-TVi and RDPV-TVa reach comparable, if not better, performances than tRCAN, and all the other unsupervised methods DPV and RDPV. Finally, a visualization of frame reconstruction provided by tRCAN alongside the best of the proposed methods, i.e., RDPV-TVi, and the GT and LR versions, is provided in Fig. S4 and S5 for Videos Type 1 and Type 2, respectively. The close-ups in the central regions occupied by the tumor cells are highlighted by red squares. We can observe how the

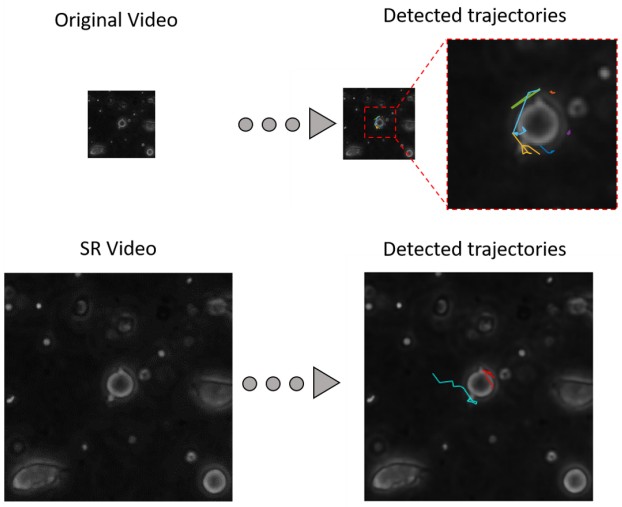

Figure 14: Visual representation of detected trajectories by Cell Hunter software on the original LR video and on the SR video reconstructed by the proposed RDPV-TVi method.

reconstruction provided by RDPV-TVi better enhances the shape of the immune and cancer cells if compared to the LR image and the tRCAN reconstruction.

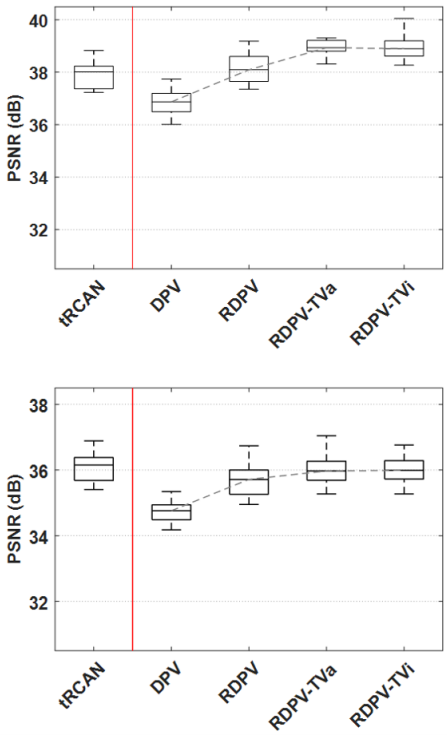

Figure 15: **Quantitative results in terms of PSNR on Videos Type 1 and on Videos Type 2.** Boxplots comprise the average values of PSNR computed over all the frames of the 10 videos Type 1 (upper panel) or videos Type 2 (lower panel). In the upper panel, tRCAN indicates RCAN trained on Videos Type 2 and some synthetic videos. In the lower panel, tRCAN indicates RCAN trained on Videos Type 1 and some synthetic videos.

6 Conclusions

In this work, we present a novel approach called Recursive Deep Prior Video to overcome the limitation of low resolution in time-lapse microscopy scenario for organ-on-chip applications, within the so-called super-resolution context. The main novelties of the approach refer to the recursive initialization of the weights of the DIP network architecture combined with an efficient early stopping criterion. In addition, the DIP loss function has been penalized by two different Total Variation-based terms. The method has been validated on synthetic, i.e., artificially generated, as well as real videos from OOC experiments related to tumor-immune interaction and compared to the most effective state of the art approaches in the context of trained methods and compared to the proposed extension of DIP for videos (DPV). The proposed approach demonstrates to be feasible to real-time applications due to the unsupervised architecture, robust to noise thanks to the regularization terms, and able to effectively work in combination with state-of-the-art edge localization and edge detection methods for the task of object recognition and biological experiment characterization. Future works will address the problem of improving the effectiveness of the approach in terms of parallelization and of implementation in the routine use of microfluidic devices to accelerate the uptake of OOC experiments.

Acknowledgments

P.C. and E.L.P. have been partially supported by the GNCS-INDAM project 2020.

References

[1] Alessandro Polini, Ljupcho Prodanov, Nupura S Bhise, Vijayan Manoharan, Mehmet R Dokmeci, and Ali Khademhosseini. Organs-on-a-chip: a new tool for drug discovery. *Expert opinion on drug discovery*, 9(4):335–352, 2014.

[2] Alexandre J Kabla. Collective cell migration: leadership, invasion and segregation. *Journal of The Royal Society Interface*, 9(77):3268–3278, 2012.

[3] Luca Businaro, Adele De Ninno, Giovanna Schiavoni, Valeria Lucarini, Gabriele Ciasca, Annamaria Gerardino, Filippo Belardelli, Lucia Gabriele, and Fabrizio Mattei. Cross talk between cancer and immune cells: exploring complex dynamics in a microfluidic environment. *Lab on a Chip*, 13(2):229–239, 2013.

[4] Elena Agliari, Elena Biselli, Adele De Ninno, Giovanna Schiavoni, Lucia Gabriele, Anna Gerardino, Fabrizio Mattei, Adriano Barra, and Luca Businaro. Cancer-driven dynamics of immune cells in a microfluidic environment. *Scientific reports*, 4(1):1–15, 2014.

[5] Tanya J Shaw and Paul Martin. Wound repair at a glance. *Journal of cell science*, 122(18):3209–3213, 2009.

[6] Peter Friedl and Darren Gilmour. Collective cell migration in morphogenesis, regeneration and cancer. *Nature reviews Molecular cell biology*, 10(7):445–457, 2009.

[7] Peter Friedl and Katarina Wolf. Tumour-cell invasion and migration: diversity and escape mechanisms. *Nature reviews cancer*, 3(5):362–374, 2003.

[8] Elena Biselli, Elena Agliari, Adriano Barra, Francesca Romana Bertani, Annamaria Gerardino, Adele De Ninno, Arianna Mencattini, Davide Di Giuseppe, Fabrizio Mattei, Giovanna Schiavoni, et al. Organs on chip approach: a tool to evaluate cancer-immune cells interactions. *Scientific reports*, 7(1):1–12, 2017.

[9] Marie Nguyen, Adele De Ninno, Arianna Mencattini, Fanny Mermet-Meillon, Giulia Fornabaio, Sophia S Evans, Mélissande Cossutta, Yasmine Khira, Weijing Han, Philémon Sirven, et al. Dissecting effects of anti-cancer drugs and cancer-associated fibroblasts by on-chip reconstitution of immunocompetent tumor microenvironments. *Cell reports*, 25(13):3884–3893, 2018.

[10] Christian Payer, Darko Štern, Marlies Feiner, Horst Bischof, and Martin Urschler. Segmenting and tracking cell instances with cosine embeddings and recurrent hourglass networks. *Medical image analysis*, 57:106–119, 2019.

[11] Assaf Arbelle, Jose Reyes, Jia-Yun Chen, Galit Lahav, and Tammy Riklin Raviv. A probabilistic approach to joint cell tracking and segmentation in high-throughput microscopy videos. *Medical image analysis*, 47:140–152, 2018.

[12] Davide Di Giuseppe, Francesca Corsi, Arianna Mencattini, Maria Colomba Comes, Paola Casti, Corrado Di Natale, Lina Ghibelli, and Eugenio Martinelli. Learning cancer-related drug efficacy exploiting consensus in coordinated motility within cell clusters. *IEEE Transactions on Biomedical Engineering*, 66(10):2882–2888, 2019.

[13] Stefania Parlato, Adele De Ninno, Rosa Molfetta, Elena Toschi, Debora Salerno, Arianna Mencattini, Giulia Romagnoli, Alessandra Fragale, Lorenzo Roccazzello, Maria Buoncervello, et al. 3d microfluidic model for

evaluating immunotherapy efficacy by tracking dendritic cell behaviour toward tumor cells. *Scientific reports*, 7(1):1–16, 2017.

[14] M. C Comes, P. Casti, A. Mencattini, D. Di Giuseppe, F. Mermet-Meillon, A. De Ninno, M. C. Parrini, L. Businaro, C. Di Natale, and E. Martinelli. The influence of spatial and temporal resolutions on the analysis of cell-cell interaction: a systematic study for time-lapse microscopy applications. *Scientific Reports*, 9:1–11, 2019.

[15] Joost B Beltman, Athanasius FM Marée, and Rob J De Boer. Analysing immune cell migration. *Nature Reviews Immunology*, 9(11):789–798, 2009.

[16] Linwei Yue, Huanfeng Shen, Jie Li, Qiangqiang Yuan, Hongyan Zhang, and Liangpei Zhang. Image super-resolution: The techniques, applications, and future. *Signal Processing*, 128:389–408, 2016.

[17] Bee Lim, Sanghyun Son, Heewon Kim, Seungjun Nah, and Kyoung Mu Lee. Enhanced deep residual networks for single image super-resolution. In *Proceedings of the IEEE conference on computer vision and pattern recognition workshops*, pages 136–144, 2017.

[18] Yulun Zhang, Kunpeng Li, Kai Li, Lichen Wang, Bineng Zhong, and Yun Fu. Image super-resolution using very deep residual channel attention networks. In *Proceedings of the European Conference on Computer Vision (ECCV)*, pages 286–301, 2018.

[19] Yifan Wang, Federico Perazzi, Brian McWilliams, Alexander Sorkine-Hornung, Olga Sorkine-Hornung, and Christopher Schroers. A fully progressive approach to single-image super-resolution. In *Proceedings of the IEEE Conference on Computer Vision and Pattern Recognition Workshops*, pages 864–873, 2018.

[20] Xintao Wang, Ke Yu, Shixiang Wu, Jinjin Gu, Yihao Liu, Chao Dong, Yu Qiao, and Chen Change Loy. ESRGAN: Enhanced super-resolution generative adversarial networks. In *Proceedings of the European Conference on Computer Vision (ECCV)*, pages 0–0, 2018.

[21] Daniele Ravì, Agnieszka Barbara Szczotka, Stephen P Pereira, and Tom Vercauteren. Adversarial training with cycle consistency for unsupervised super-resolution in endomicroscopy. *Medical image analysis*, 53:123–131, 2019.

[22] Andrea Rueda, Norberto Malpica, and Eduardo Romero. Single-image super-resolution of brain mr images using overcomplete dictionaries. *Medical image analysis*, 17(1):113–132, 2013.

[23] Jithin Saji Isaac and Ramesh Kulkarni. Super resolution techniques for medical image processing. In *2015 International Conference on Technologies for Sustainable Development (ICTSD)*, pages 1–6. IEEE, 2015.

[24] Pasquale Cascarano, Francesco Corsini, Stefano Gandolfi, Elena Loli Piccolomini, Emanuele Mandanici, Luca Tavasci, and Fabiana Zama. Super-resolution of thermal images using an automatic total variation based method. *Remote Sensing*, 12(10):1642, 2020.

[25] Rafael E Rivadeneira, Patricia L Suárez, Angel D Sappa, and Boris X Vintimilla. Thermal image superresolution through deep convolutional neural network. In *International Conference on Image Analysis and Recognition*, pages 417–426. Springer, 2019.

[26] Daiqin Yang, Zimeng Li, Yatong Xia, and Zhenzhong Chen. Remote sensing image super-resolution: Challenges and approaches. In *2015 IEEE international conference on digital signal processing (DSP)*, pages 196–200. IEEE, 2015.

[27] Frank Lin, Clinton Fookes, Vinod Chandran, and Subramanian Sridharan. Investigation into optical flow super-resolution for surveillance applications. In *WDIC 2005: APRS Workshop on Digital Image Computing: Workshop Proceedings:*, pages 73–78. University of QLD, 2005.

[28] Bonnie O Leung and Keng C Chou. Review of super-resolution fluorescence microscopy for biology. *Applied spectroscopy*, 65(9):967–980, 2011.

[29] Antoine G Godin, Brahim Lounis, and Laurent Cognet. Super-resolution microscopy approaches for live cell imaging. *Biophysical journal*, 107(8):1777–1784, 2014.

[30] Hongda Wang, Yair Rivenson, Yiyin Jin, Zhensong Wei, Ronald Gao, Harun Günaydın, Laurent A Bentolila, Comert Kural, and Aydogan Ozcan. Deep learning enables cross-modality super-resolution in fluorescence microscopy. *Nature methods*, 16(1):103–110, 2019.

[31] Martin Weigert, Uwe Schmidt, Tobias Boothe, Andreas Müller, Alexandr Dibrov, Akanksha Jain, Benjamin Wilhelm, Deborah Schmidt, Coleman Broaddus, Siân Culley, et al. Content-aware image restoration: pushing the limits of fluorescence microscopy. *Nature methods*, 15(12):1090–1097, 2018.

[32] Dmitry Ulyanov, Andrea Vedaldi, and Victor S. Lempitsky. Deep image prior. *CoRR*, abs/1711.10925, 2017.

[33] Jiaming Liu, Yu Sun, Xiaojian Xu, and Ulugbek S Kamilov. Image restoration using total variation regularized deep image prior. In *ICASSP 2019-2019 IEEE International Conference on Acoustics, Speech and Signal Processing (ICASSP)*, pages 7715–7719. IEEE, 2019.

[34] L I Rudin, S Osher, and E Fatemi. Nonlinear total variation based noise removal algorithms. *Physica D: Nonlinear Phenomena*, 60(1-4):259–268, 1992.

[35] Alain Hore and Djemel Ziou. Image quality metrics: Psnr vs. ssim. In *2010 20th international conference on pattern recognition*, pages 2366–2369. IEEE, 2010.

[36] Claude E Duchon. Lanczos filtering in one and two dimensions. *Journal of applied meteorology*, 18(8):1016–1022, 1979.

[37] Zhihao Wang, Jian Chen, and Steven CH Hoi. Deep learning for image super-resolution: A survey. *IEEE Transactions on Pattern Analysis and Machine Intelligence*, 2020.

[38] Hongying Liu, Zhubo Ruan, Peng Zhao, Fanhua Shang, Linlin Yang, and Yuanyuan Liu. Video super resolution based on deep learning: A comprehensive survey. *arXiv preprint arXiv:2007.12928*, 2020.

[39] Diederik P Kingma and Jimmy Ba. ADAM: A method for stochastic optimization. *arXiv preprint arXiv:1412.6980*, 2014.

[40] Erika Vacchelli, Yuting Ma, Elisa E Baracco, Antonella Sistigu, David P Enot, Federico Pietrocola, Heng Yang, Sandy Adjemian, Kariman Chaba, Michaela Semeraro, et al. Chemotherapy-induced antitumor immunity requires formyl peptide receptor 1. *Science*, 350(6263):972–978, 2015.

[41] Néstor Sepúlveda, Laurence Petitjean, Olivier Cochet, Erwan Grasland-Mongrain, Pascal Silberzan, and Vincent Hakim. Collective cell motion in an epithelial sheet can be quantitatively described by a stochastic interacting particle model. *PLoS Comput Biol*, 9(3):e1002944, 2013.

[42] E Roy Davies. *Machine vision: theory, algorithms, practicalities*. Elsevier, 2004.

[43] James Munkres. Algorithms for the assignment and transportation problems. *Journal of the society for industrial and applied mathematics*, 5(1):32–38, 1957.

[44] Gabriele Di Sante, Mathew C Casimiro, Timothy G Pestell, and Richard G Pestell. Time-lapse video microscopy for assessment of eyfp-parkin aggregation as a marker for cellular mitophagy. *JoVE (Journal of Visualized Experiments)*, (111):e53657, 2016.

[45] Richard A Haddad, Ali N Akansu, et al. A class of fast gaussian binomial filters for speech and image processing. *IEEE Transactions on Signal Processing*, 39(3):723–727, 1991.

[46] Johannes Huth, Malte Buchholz, Johann M Kraus, Martin Schmucker, Götz Von Wichert, Denis Krndija, Thomas Seufferlein, Thomas M Gress, and Hans A Kestler. Significantly improved precision of cell migration analysis in time-lapse video microscopy through use of a fully automated tracking system. *BMC cell biology*, 11(1):24, 2010.

[47] Dominique Ernst, Jürgen Köhler, and Matthias Weiss. Probing the type of anomalous diffusion with single-particle tracking. *Physical Chemistry Chemical Physics*, 16(17):7686–7691, 2014.

[48] Josep L Carrasco and Lluis Jover. Estimating the generalized concordance correlation coefficient through variance components. *Biometrics*, 59(4):849–858, 2003.

[49] Nikolaos P Galatsanos SAAAS Aggelos Katsaggelos. Methods for choosing the regularization parameter and estimating the noise variance in image restoration and their relation. *IEEE Transactions on image processing*, 1(3), 1992.

[50] Robert Keys. Cubic convolution interpolation for digital image processing. *IEEE transactions on acoustics, speech, and signal processing*, 29(6):1153–1160, 1981.

[51] John Canny. A computational approach to edge detection. *IEEE Transactions on pattern analysis and machine intelligence*, (6):679–698, 1986.